Open Research Online

The Open University's repository of research publications
and other research outputs

Geology of the Victoria quadrangle (H02), Mercury

Journal Item

oro.open.ac.uk

Geology of the Victoria quadrangle (H02), Mercury

V. Galluzzi, L. Guzzetta, L. Ferranti, G. Di Achille, D. A. Rothery & P. Palumbo

Taylor & Francis
Taylor & Francis Group

Geology of the Victoria quadrangle (H02), Mercury

V. Galluzzi[a] , L. Guzzetta[a], L. Ferranti[b], G. Di Achille[c] , D. A. Rothery[d] and P. Palumbo[a,e]

[a]INAF, Istituto di Astrofisica e Planetologia Spaziali, Rome, Italy; [b]DiSTAR, Università degli Studi di Napoli 'Federico II', Naples, Italy; [c]INAF, Osservatorio Astronomico di Teramo, Teramo, Italy; [d]Department of Physical Sciences, The Open University, Milton Keynes, UK; [e]Dipartimento di Scienze e Tecnologie, Università degli Studi di Napoli 'Parthenope', Naples, Italy

ABSTRACT

Mercury's quadrangle H02 'Victoria' is located in the planet's northern hemisphere and lies between latitudes 22.5° N and 65° N, and between longitudes 270° E and 360° E. This quadrangle covers 6.5% of the planet's surface with a total area of almost 5 million km². Our 1:3,000,000-scale geologic map of the quadrangle was produced by photo-interpretation of remotely sensed orbital images captured by the MESSENGER spacecraft. Geologic contacts were drawn between 1:300,000 and 1:600,000 mapping scale and constitute the boundaries of intercrater, intermediate and smooth plains units; in addition, three morpho-stratigraphic classes of craters larger than 20 km were mapped. The geologic map reveals that this area is dominated by Intercrater Plains encompassing some almost-coeval, probably younger, Intermediate Plains patches and interrupted to the north-west, north-east and east by the Calorian Northern Smooth Plains. This map represents the first complete geologic survey of the Victoria quadrangle at this scale, and an improvement of the existing 1:5,000,000 Mariner 10-based map, which covers only 36% of the quadrangle.

1. Introduction

In their first geologic map of Mercury derived from Mariner 10 (M10) imagery, Trask and Guest (1975) introduced the concept of 'terrain units' asserting that '[…] on Mercury, surface morphology reflects the age, composition, lithology, and mode of formation of the underlying rock unit' (p. 2461). Terrain units of Mercury were revisited during geologic mapping of Mercury at 1:5,000,000 scale, based on M10 images (De Hon, Scott, & Underwood, 1981; Grolier & Boyce, 1984; Guest & Greeley, 1983; King & Scott, 1990; McGill & King, 1983; Schaber & McCauley, 1980; Spudis & Prosser, 1984; Strom, Malin, & Leake, 1990; Trask & Dzurisin, 1984; merged maps, Frigeri, Federico, Pauselli, & Coradini, 2009) and termed 'geologic provinces' by Spudis and Guest (1988), who adopted this term to denote regional scale areas 'characterized by a similar inferred origin or a distinctive history' (McCauley & Wilhelms, 1971, p. 363).

For the M10 geologic mapping project, Mercury was officially divided into 15 quadrangles (see Davies, Dwornik, Gault, & Strom, 1978) named after prominent topographic features where M10 coverage data were available, and telescopic albedo features elsewhere. Global coverage by the MESSENGER mission (orbit 2011–2015) enabled all quadrangles to be named after topographic features.

Victoria quadrangle (270°E–360°E; 22.5°N–65°N) is named after a lobate scarp at ∼340°E longitude that is its most prominent feature. Victoria Rupes is aligned with Endeavour Rupes and Antoniadi Dorsum, and altogether form a ∼900 km long N–S striking fault system interpreted as a fold-and-thrust belt by Byrne et al. (2014).

In the first geologic map by McGill and King (1983), more than 60% of Victoria quadrangle remained unmapped because of the lack of M10 basemap images. Recently, the MESSENGER team has completed a 1:15,000,000-scale global geologic map of Mercury (Prockter et al., 2016), covering all previously unmapped regions. Here we exploit the available MESSENGER data to make a geological survey of the Victoria Quadrangle at a scale of 1:3,000,000.

2. Data

2.1. Basemaps

The most up to date imaging data for Mercury were acquired by the MESSENGER spacecraft and, in particular, by its Mercury Dual Imaging System (MDIS), comprising a wide angle camera (WAC) and a narrow angle camera (NAC) that acquired more than 270,000 images (see: http://messenger.jhuapl.edu). Both cameras covered the planet with a mean resolution of ∼200 m/pixel (surface covered: MDIS/WAC, 100%; MDIS/NAC, 100% southern hemisphere, 60% northern hemisphere) reaching a maximum of ∼8 m/pixel with MDIS/NAC (see: http://pds-imaging.jpl.nasa.gov/).

This article was originally published with errors. This version has been corrected. Please see Corrigendum (http://dx.doi.org/10.1080/17445647.2016.1209878)

Table 1. List of used basemaps.

#	Original basemap	Resolution (m/pixel)	Source
1	MDIS_BDR_256PPD_Hxxdd[a]	166	http://pds-imaging.jpl.nasa.gov/data/messenger/msgrmds_4001/
2	20130514_complete_mono_basemap	250	http://messenger.jhuapl.edu/the_mission/mosaics.html
3	MDIS_v8_750nm_250mpp	250	http://messenger.jhuapl.edu/the_mission/mosaics.html
4	MDIS_v7_mono_250mpp	250	http://messenger.jhuapl.edu/the_mission/mosaics.html
5	MDIS_v6_mono_250mpp	250	http://messenger.jhuapl.edu/the_mission/mosaics.html
6	M1_M2_M3_M10Filt (Becker et al., 2009)	500	http://astrogeology.usgs.gov/maps/mercury-messenger-global-mosaic
7	MESSENGER_color_mono[b]	200	ftp://pdsimage2.wr.usgs.gov/pub/pigpen/mercury/
8	usgs_20110913_albedo[b]	200	ftp://pdsimage2.wr.usgs.gov/pub/pigpen/mercury/
9	MDIS_v0_3color (MD3 basemap)	332	http://messenger.jhuapl.edu/the_mission/mosaics.html
10	MDIS_v5_8color (MDR basemap)	665	http://messenger.jhuapl.edu/the_mission/mosaics.html
11	M10 Mercury Mosaic (Calibrated)	1000	http://ser.sese.asu.edu/M10/IMAGE_ARCHIVE/MOSAICS/
12	M10 Mercury Shaded Relief	1330	http://ser.sese.asu.edu/M10/IMAGE_ARCHIVE/MOSAICS/

[a]xx indicates the quadrangles and dd indicates the tiles NP, NW, NE, SE, SE shown in Figure 1.
[b]MercuryGIS_DVD_v03 previously available at USGS FTP.

A schematic summary of the image-derived basemaps used in this project is shown in Table 1. The listing from top to bottom reflects the priority order, principally based on image resolution.

To date, no highly controlled base (e.g. such as the Lunar Orbiter Laser Altimeter data) has been released for Mercury, and our basemaps show some discrepancies and are not perfectly georeferenced to each other. The map-projected Basemap reduced Data Record (BDR) products have with the highest available resolution (∼166 m/pixel, Murchie et al., 2016), thus they were considered as a reference basemap.

H02 has no overlap with the adjacent quadrangles but we worked with a 5° for better interpretation of features near the quadrangle's edges. Thus, we mosaicked 13 BDR tiles to obtain our complete BDR reference basemap in Figure 1.

Most of the basemaps listed in Table 1 were obtained during the basemap imaging campaign of MESSENGER's primary mission and they mostly use the same source frames. Nonetheless, there are some areas were different mosaic tiles were used, sometimes showing different lighting conditions (e.g. note the difference between the eastern and the western area in Figure 1). Use of several lighting directions is useful

in mapping, because it reduces bias while defining structures.

The first global mosaic of Mercury was released by the United States Geological Survey (USGS) soon after the three MESSENGER flybys (i.e. M1, M2 and M3; Becker et al., 2009). This near global mosaic of the planet (∼97%) at 500 m/pixel resolution represents an important source of data because it offers strong shadow contrasts in the western region of H02 despite its low resolution. This is particularly important for detecting structures that are obscure in the low-incidence angle western area of the BDR basemap.

The 8-color map-projected Multispectral reduced Data Record (MDR) and the 3-Color map-projected Multispectral reduced Data Record (MD3) mosaics (Table 1) do not offer a good resolution for mapping features, but are useful to verify contacts that were photo-interpreted from monochrome images; in fact, some Hermian geologic provinces are distinguishable also from their distinctive colours (Denevi et al., 2009; Ernst et al., 2010; Prockter et al., 2010). Colour variations for both MDR and the MD3 basemaps are best seen when using red: 996 nm, green: 749 nm and blue: 433 nm. We relied on the MDR basemap only when the MD3 higher resolution coverage was unavailable.

M10 basemaps were used as an historical record of the past mission. Although their resolution is very low and the coverage is poor, they are useful for comparing with the McGill and King (1983) geologic map.

The BDR basemap associated with the other basemaps in Table 1 provided enough information for mapping the whole quadrangle, but several issues arose from their uneven appearance. Figure 1 shows that the reference basemap is missing some tiles, especially in its eastern part. These gaps are covered by the other basemaps but with a lower resolution. Extremely high incidence angles cause long shadows that can hide important features (e.g. irregular pits inside crater floors), whereas extremely low-incidence angles can fail to reveal topographic features such as faults. We partially circumvented these issues by toggling the visibility of each basemap to compare them
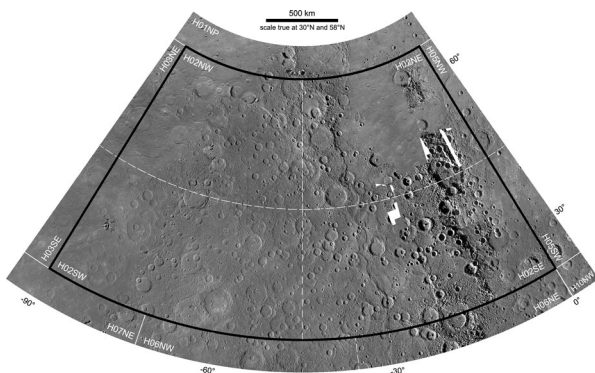

Figure 1. Mosaicked BDR basemap (∼166 m/pixel) of the Victoria quadrangle of Mercury in LCC projection with 5° overlap. Thick black line: actual H02 boundary; solid white lines: other quadrangle boundaries; dashed white lines: BDR tile boundaries (including names).
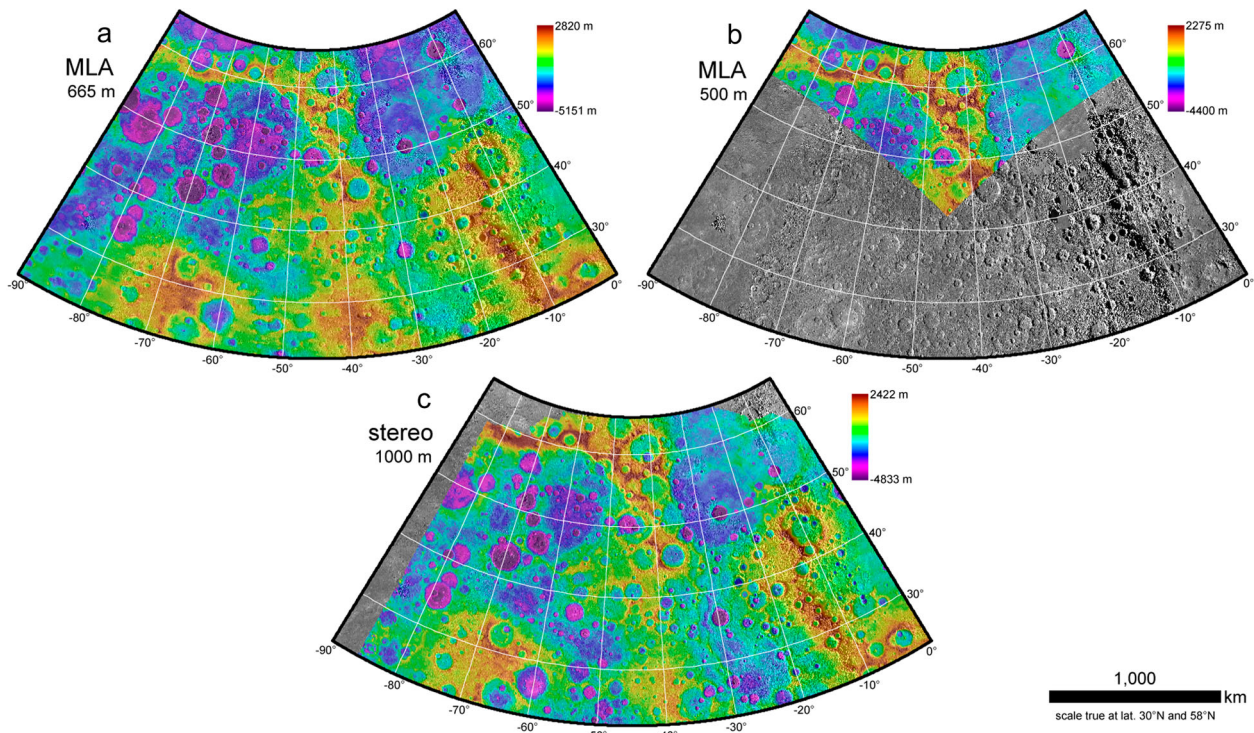
Figure 2. Topography available for the H02 quadrangle. (a) MLA coverage (Zuber et al., 2012). (b) MLA north pole coverage (Zuber et al., 2012). (c) Stereo DTM 'M2' coverage by Preusker et al. (2011).

and lower the biases deriving from lighting conditions. However, when necessary, we used single frames or generated local mosaics.

2.2. Topography

Topographic information for Mercury was gathered through two separate MESSENGER sources: (1) Mercury Laser Altimeter (MLA) data (Zuber et al., 2012) and (2) Deutsche Zentrum für Luft- und Raumfahrt, German Aerospace Center (DLR) stereo-mosaics (Preusker et al., 2011).

The MLA data sets by Zuber et al. (2012) provide 665 m spatial resolution coverage of the entire quadrangle (Figure 2(a)) and a 500 m spatial resolution coverage of the North Pole (Figure 2(b)). However, the 665 m layer is affected by a decrease in quality towards the south of H02 because of the widening spacing between MLA tracks (up to ∼100 km at 22.5°N). The DLR stereo-topography is a product of three MESSENGER flybys (M1, M2 and M3) that covered 30% of the planet with a spatial resolution of 1000 m (Preusker et al., 2011). About 80% of the Victoria quadrangle is covered by the M2 stereo-mosaic as shown in Figure 2(c).

3. Methods

3.1. Projection

Victoria quadrangle is located at mid-latitudes where it is conventional to use a Lambert Conformal Conic (LCC) projection (see Davies et al., 1978). This uses two standard parallels that represent the secants between the sphere and the cone of projection, conventionally at d of 1/6 and 5/6 of the latitudinal range (Deetz & Adams, 1945). When the H02 quadrangle was first defined, its latitudinal range was 20° N–70°N so the standard parallels were fixed at 30°N and 60°N (McGill & King, 1983). Because of the newly defined post-MESSENGER latitudinal boundaries (i.e. 22.5°N–65°N), the second standard parallel is now 58°N.

The scale of features is true along the standard parallels, slightly smaller between them and slightly larger beyond them. As a reference datum we used a sphere with a radius of 2440 km as often used in the data released by the MESSENGER team.

3.2. Mapping and final output scales

To obtain the final output scale of 1:3,000,000 shown in the Main Map, we used a mapping scale based on both USGS guidelines and raster resolution. The mapping scale is the scale at which it is recommended to draw lines. USGS guidelines suggest drawing contacts at a scale two to five times larger than the final output scale (Tanaka, Skinner, & Hare, 2011). Generally, drawing contacts at a scale five times larger generates cleaner and smoother linework. Following this rule, a 1:3,000,000 map could be generated using a mapping scale of 1:600,000. However, another common rule for choosing the mapping scale was defined by Tobler (1987), saying that $Sm = Rr \times 2000$, where Sm is the mapping scale and Rr the raster resolution; thus, the

features on the BDR reference basemap (∼166 m/pixel) could be drawn at a scale of ∼1:300,000. Taking into consideration both rules, the variability of the used basemap resolution (Table 1) and the uneven appearance of most basemap mosaics, the we drew contacts at a variable scale between ∼1:300,000 and ∼1:600,000.

3.3. Geodatabase structure and line drawing

We organised vector layers (i.e. feature classes) for digitising using a geographic information system (GIS) geodatabase, following most of the USGS recommendations and established features. In particular, we used three main feature classes: (1) geologic contacts (i.e. polyline layer); (2) linear features (i.e. polyline layer) and (3) surface features (i.e. polygon layer).

Geologic contacts define boundaries between the various geologic units and crater material classes. They constitute the main digitising layer since they were converted to polygons during map finalisation. They were divided into: (a) certain, where there is a clear and sharp contrast between terrain textures or morphologies and (b) approximate, where there is an uncertain, unclear or gradational transition between terrains.

Linear features include faults, wrinkle ridges, crater rim crests and volcanic structures. Faults were divided into two categories: (a) thrusts and (b) contractional faults (no extensional faults are apparent in this region). Both categories were divided into certain in case of clear segment traces and uncertain where segments were inferred scarp shadows. Common morphologies such as *lobate scarps* (see Massironi, Byrne, & van der Bogert, 2015) and *high-relief ridges* (see Massironi & Byrne, 2015) were mapped as thrusts. Structures showing no significant break in slope nor a lobate trace were assigned to the 'contractional fault' category, based on the observation of the dominant contractional nature of Mercury tectonics (e.g. Byrne et al., 2014; Di Achille et al., 2012). *Wrinkle ridges* (see Korteniemi, Walsh, & Hughes, 2015), although they are considered a 'contractional feature', were mapped separately as they are typically located within smooth plains (SP; e.g. Byrne et al., 2014).

We used different symbologies for craters according to their size. Craters with diameter >20 km were mapped as standard craters, meaning that they are characterised by a geologic contact defining their material boundaries (e.g. ejecta and central peaks). Their rims were denoted by ornamental ticks facing the steep inner scarp. We classified craters with diameters of 5–20 km as 'small craters', and did not record any geologic contact defining their deposits. Craters, or parts of them, whose rim crest is still visible but profoundly degraded or covered by other units were mapped as 'buried or degraded craters'. Surface features include secondary crater clusters

and chains, and clusters of *hollows* (see Blewett, 2015). Hollows are features peculiar to Mercury; they are flat-floored irregular and rimless depressions, surrounded by high-reflectance material, probably caused by volatile loss (Blewett et al., 2011; Thomas, Rothery, Conway, & Anand, 2014a). Considering their small size, we mapped only the brighter and larger clusters (>10 km long), consistent with the larger hollow groups collected in the database of Thomas et al. (2014a). Following USGS recommendations (Tanaka et al., 2011), our mapping scale led us to avoid digitising outcrops (e.g. central peaks) smaller than 4 km.

4. Map description

4.1. Crater material classification

Since craters are progressively degraded over time, mostly by subsequent impacts, many authors have tried to use morphological evidence to classify crater degradation and assess their relative ages (e.g. Arthur, Agnieray, Horvath, Wood, & Chapman, 1963; Baker & Head, 2013; Cintala, Head, & Mutch, 1976; Leake, 1982; McCauley, Guest, Schaber, Trask, & Greeley, 1981; Pohn & Offield, 1970; Spudis & Guest, 1988; Wood, 1979; Wood & Anderson, 1978; Wood, Head, & Cintala, 1977). The M10 geological mapping project used a crater classification system with five classes of craters (McCauley et al., 1981): M10/C1 are the oldest and most degraded craters, while M10/C5 are the youngest and least degraded craters. The ascending class order from subdued to crisp craters was chosen to reflect a normal stratigraphic order. Recently, Kinczyk, Prockter, Chapman, and Susorney (2016) revisited this crater classification using MESSENGER (M) data; they inverted the class order (M/C1 fresh, M/C5 very degraded) and assigned each crater class to a corresponding division of the global stratigraphy.

However, the resolution of MESSENGER images highlights a diversity of crater morphologies at our mapping scale. The relationship between crater relative age and crater degradation is not always direct and straightforward. Morphological differences among craters that we mapped in H02, depend on both their relative age and their size. Smaller craters reach a higher level of degradation more quickly than larger craters. Moreover, isolated craters experience less degradation than overlapping or adjacent craters. Relying on a pure morphological classification of craters, with a high number of classes, could thus lead to a stratigraphic misinterpretation of impact events. We elected to distinguish only three crater classes, in order to reduce the error in assigning relative ages, based on a crater's morphological appearance. This avoided contradictions encountered in the five-class scheme, in
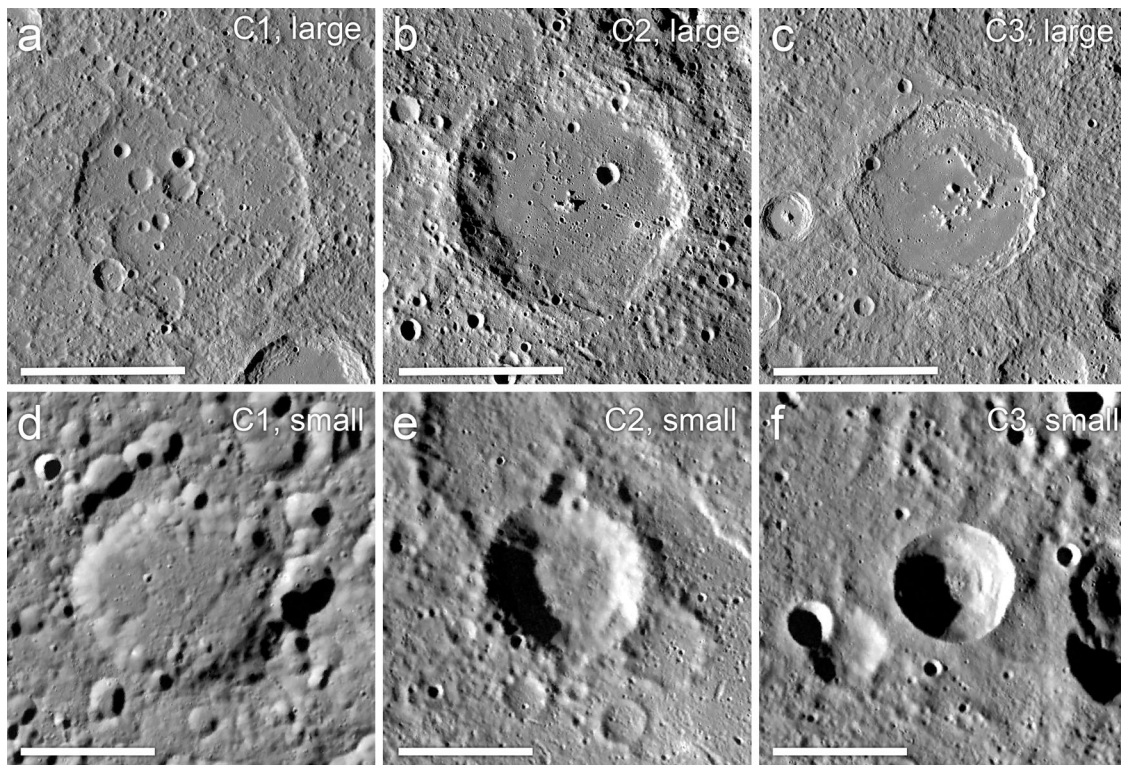
Figure 3. Type localities of the three used crater classes for large ((a)–(c), scale bar is 100 km) and small ((d)–(f), scale bar is 20 km) craters inside the H02 quadrangle (on the BDR basemap, ~166 m/pixel). (a) Kuan Han-Ch'ing crater at 310.27°E, 30.80°N. (b) Derzhavin crater at 323.10°E, 45.59°N. (c) Velázquez crater at 304.77°E, 37.74°N. (d) Unnamed crater at 289.29°E, 36.40°N. (e) Unnamed crater at 325.4°E, 40.80°N. (f) Unnamed crater at 320.03°E, 41.43°N. See also the 'Description of map units' section for a detailed description of the three classes.

which morphologically 'older' craters sometimes overlie morphological 'younger' craters.

We defined our three-class morpho-stratigraphic system by the type examples from within H02 shown in Figure 3. Class 3 and class 1 represent two end-member cases for the youngest and oldest craters, respectively, while class 2 encompasses all the other intermediate cases. The rim sharpness (from sharp and continuous to subdued and discontinuous), the texture of the ejecta blanket (from textured ejecta to subdued or absent ejecta) and the secondary crater density inside crater floors (from poorly cratered to intensely cratered) are the key attributes used in assigning craters to each class. We defined this scheme for this quadrangle only since we made no global crater survey, though it could form the basis of a relative-age classification scheme to be used planet-wide.

4.2. Mapped geologic provinces

In this quadrangle, we mapped three main geologic provinces: intercrater plains (ICP), intermediate plains (IMP) and SP.

4.2.1. Intercrater plains

Trask and Guest (1975, p. 2463) defined the ICP as 'level to gently rolling ground between and around large craters and basins' (Figure 4). This is the most widespread unit on Mercury and is thought to be the remnants of volcanic flows by most authors (Denevi et al., 2016; Kiefer & Murray, 1987; Murray et al., 1974, 1975; Spudis & Guest, 1988; Strom, 1977; Trask & Guest, 1975; Whitten, Head, Denevi, & Solomon, 2014). The emplacement of ICP predates the end of the Late Heavy Bombardment (e.g. Trask & Guest, 1975) of the Inner Solar System, thus these materials are Tolstojan to pre-Tolstojan (Whitten et al., 2014) and represent the oldest surface on Mercury (>3.9 Ga, Denevi et al., 2016). In the H02 quadrangle, ICP cover a larger area than any other province.

4.2.2. Intermediate plains

These terrains form 'planar to undulating surfaces that have higher crater density than SP material, but are less heavily cratered than intercrater plains material' (Spudis & Prosser, 1984). However, recent work concludes that there is no clear contrast between IMP and ICP, which seem to have a 'patchy' distribution, and the adjacent terrains (Denevi et al., 2013; Whitten et al., 2014). Despite the similarity with ICP at a regional scale, our mapping scale (i.e. ~1:450,000) allowed us to recognise localised textural changes, sometimes confirmed by colour variations (see Figure 5(a) and 5(b)). We mapped less IMP than McGill and King (1983). This is probably due to the difference in resolution between M10 and MESSENGER data. Moreover,
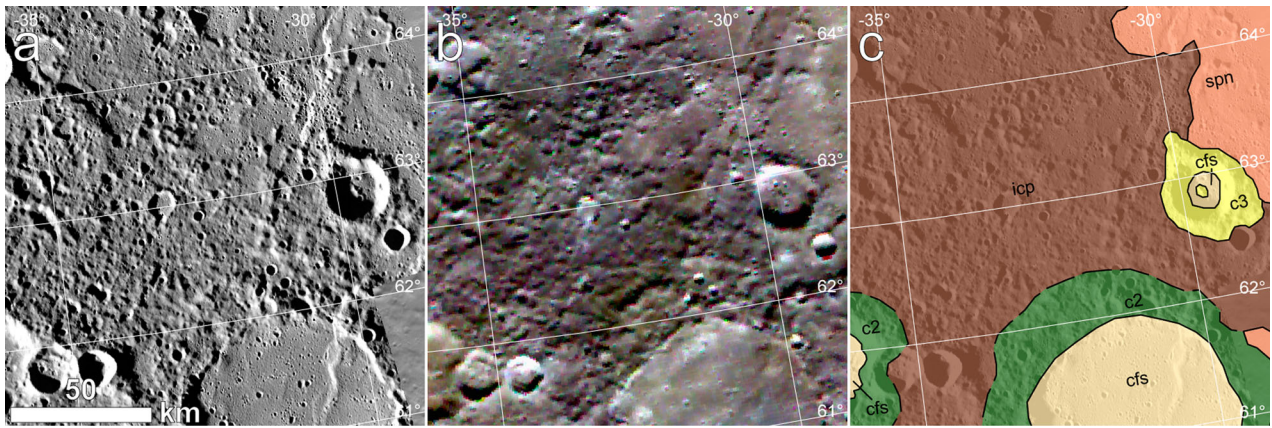
Figure 4. Example area of the ICP geologic province inside H02: (a) BDR basemap (~166 m/pixel). Here a very rough surface (ICP) is visible in the centre of the image. (b) MDR basemap (665 m/pixel). Here ICP present a slightly darker colour than SPn. (c) 1:3M geologic map showing contacts between ICP (labelled 'icp') and SPn (labelled 'spn'). See key colours in the Main Map. Projection: LCC (see text for details).

where there are gradational contacts, IMP was limited to smoother terrains, leaving areas with slightly higher crater density outside the contact. In the western region of H02, IMP are approximately located inside the high-Mg region described by Weider et al. (2015). In the eastern region, IMP correspond approximately to an area previously mapped as SP by Denevi et al. (2013), p. 894, which is characterised by high Al abundance (Weider et al., 2015). Whitten et al. (2014) state that IMP show similar ages to ICP of Tolstojan and Pre-Tolstojan period, though the lower crater density and superposition relationships (where apparent) confirm that IMP is younger than ICP.

4.2.3. Smooth plains
SP were defined for their morphological characteristics as 'relatively flat, sparsely cratered material' (Spudis & Guest, 1988; Strom, Trask, & Guest, 1975; Trask & Guest, 1975) 'that displays sharp boundaries with adjacent regions and is level to gently sloped over a baseline

of ~100–200 km' (Denevi et al., 2013, p. 894). Recently their volcanic nature was confirmed due to evidence of flow and sharp colour contrasts with adjacent units (Denevi et al., 2013). In the north polar region of Mercury, SP are known as the 'Northern smooth plains' (SPn, Denevi et al., 2013; Ostrach et al., 2015); inside the H02 quadrangle most of the mapped SP pertain to this unit (Figure 6). Several authors believe SP belong to the Calorian period estimating an age of 3.7–3.9 Ga based on crater density distribution (Denevi et al., 2013; Fassett et al., 2009; Head et al., 2011; Ostrach, Robinson, Denevi, & Thomas, 2011; Strom, Chapman, Merline, Solomon, & Head, 2008, 2011).

4.3. Description of map units
c3, crater material – well preserved: fresh craters with sharp rims. Clearly recognisable, textured ejecta blanket. Largest craters usually have radial chains of secondary craters. When central peaks or peak rings are

Figure 5. Example area of the IMP geologic province inside H02: (a) BDR basemap (~166 m/pixel). Here a slightly smoother surface is visible to the right of the image (IMP), but does not show a clear contact with the adjoining rougher surface (ICP). (b) MDR basemap (665 m/pixel). Here IMP present a slightly brighter colour than ICP. (c) 1:3M geologic map showing an approximate contact between IMP (labelled 'imp') and ICP (labelled 'icp'). See key colours in the Main Map. Projection: LCC (see text for details).
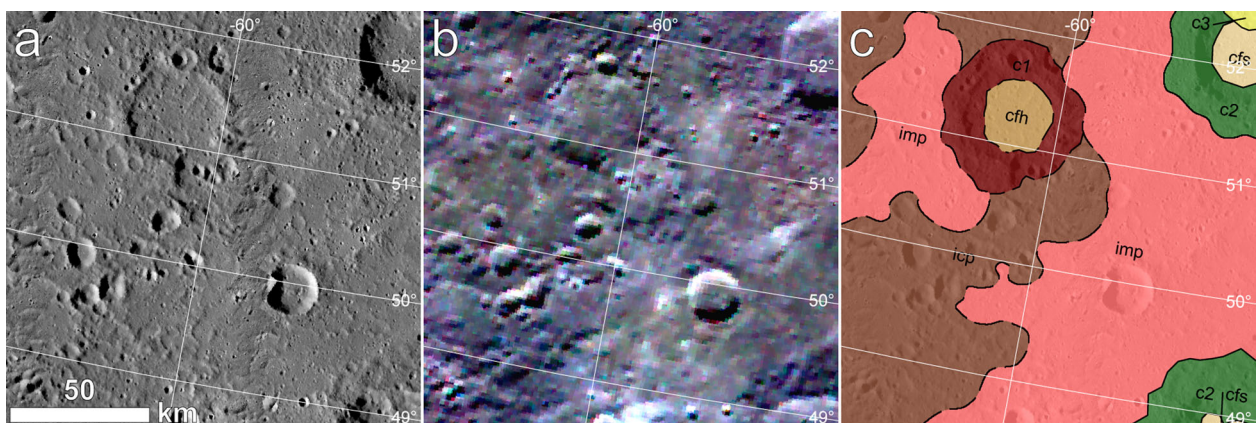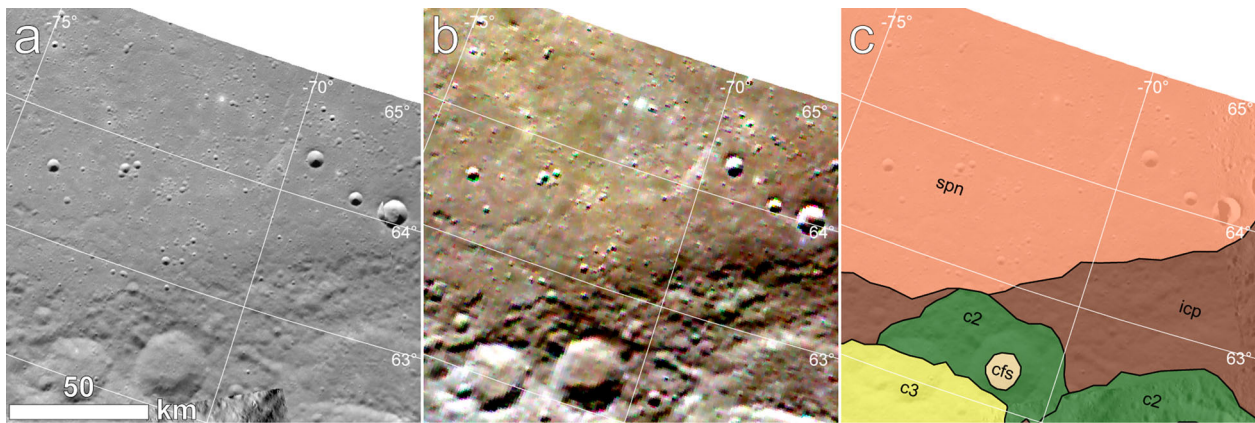
Figure 6. Example area of the SPn geologic province inside H02: (a) BDR basemap (∼166 m/pixel). Here the smooth surface to the north is clearly recognisable and has a clear, sharp boundary with the rough surface adjoining to the south. (b) MDR basemap (665 m/pixel). Here SPn has a brighter colour than ICP. (c) 1:3M geologic map showing contacts between SPn (labelled 'spn') and ICP (labelled 'icp'). See key colours in the Main Map. Projection: LCC (see text for details).

present, their boundary is sharp and well recognisable. Crater floor is pristine or sparsely cratered by <5 km craters. This class broadly corresponds to M10/C5 to M10/C4 craters of McCauley et al. (1981). *Type-areas:* 304.8°E, 37.7°N (Figure 3(c)); 320.0°E, 41.4°N (Figure 3(f)).

c2, crater material – degraded: degraded craters with subdued but still easily recognisable rims. Proximal ejecta are more recognisable than distant ejecta. They may not always present a textured ejecta blanket. Central peaks and peak rings are still recognisable. Crater floor may have smooth to hummocky morphology and is more densely cratered than *c3*. This class approximately corresponds to M10/C3 to M10/C2 craters of McCauley et al. (1981). *Type-areas:* 323.1°E, 45.6°N (Figure 3(b)); 325.4°E, 40.8°N (Figure 3(e)).

c1, crater material – heavily degraded: heavily degraded craters with subdued or discontinuous rims sometimes recognisable only with the aid of topography. Largest craters (>150 km) may still preserve recognisable proximal ejecta and internal subdued peak rings. These craters often have a hummocky and densely cratered floor. This class approximately corresponds to M10/C2 to M10/C1 craters of McCauley et al. (1981). *Type-areas:* 310.3°E, 30.80°N (Figure 3(a)); 289.3°E, 36.4°N (Figure 3(d)).

cfs, crater floor material – smooth: very smooth, planar and sparsely cratered crater floor surfaces. Mostly found inside *c3* and *c2* craters or on resurfaced floors of *c1* craters. *Type-areas:* 280.1°E, 51.6°N; 315.8°E, 31.7°N.

cfh, crater floor material – hummocky: rough or gently rolling, moderately cratered crater floor surfaces. For *c3* and *c2* craters, this unit corresponds mostly to crater wall debris, while for *c1* craters it is represented by very degraded floors. *Type-areas:* 351.0°E, 61.8°N; 351.2°E, 43.6°N.

sp, SP material: smooth and sparsely cratered planar surfaces. The boundary with adjacent materials is sharp

and easily recognisable. In H02, it is found only on small areas over crater ejecta in the form of lava pools of ejecta melts. *Type-areas:* 302.9°E, 39.2°N; 279.2°E, 50.4°N.

spn, SP material – northern: smooth and poorly cratered planar surfaces confined to the high northern latitudes of the quadrangle, superposed only by *c3* craters. The boundary is usually sharp and easily recognisable, against older crater rims, ICP material relief or tectonic features. Older underlying craters are often recognisable as 'ghost craters'. Characterised by a widespread presence of wrinkle ridges. *Type-areas:* 354.8°E, 56.1°N (Figure 6); 287.1°E, 64.5°N.

imp, IMP material: smooth undulating to planar surfaces, more densely cratered than the SP and superposed by both *c3* and *c2* craters. May have partially covered older *c1* craters. These materials always adjoin ICP material, but seldom present clear boundaries; they rather blend from smooth to rough surfaces with a gradational contact. In the eastern area of the quadrangle the undulation of these materials is caused by systematic lobate scarps. *Type-areas:* 331.4°E, 32.1°N; 301.6°E, 50.9°N (Figure 5).
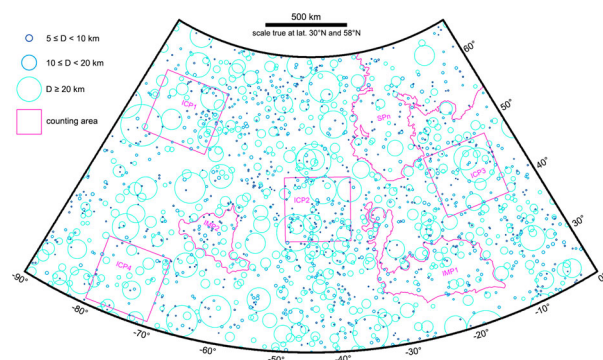

Figure 7. Database of craters larger than 5 km inside the Victoria quadrangle (different shades of blue indicate different diameter ranges). The magenta lines indicate the seven study areas where crater counting was performed.
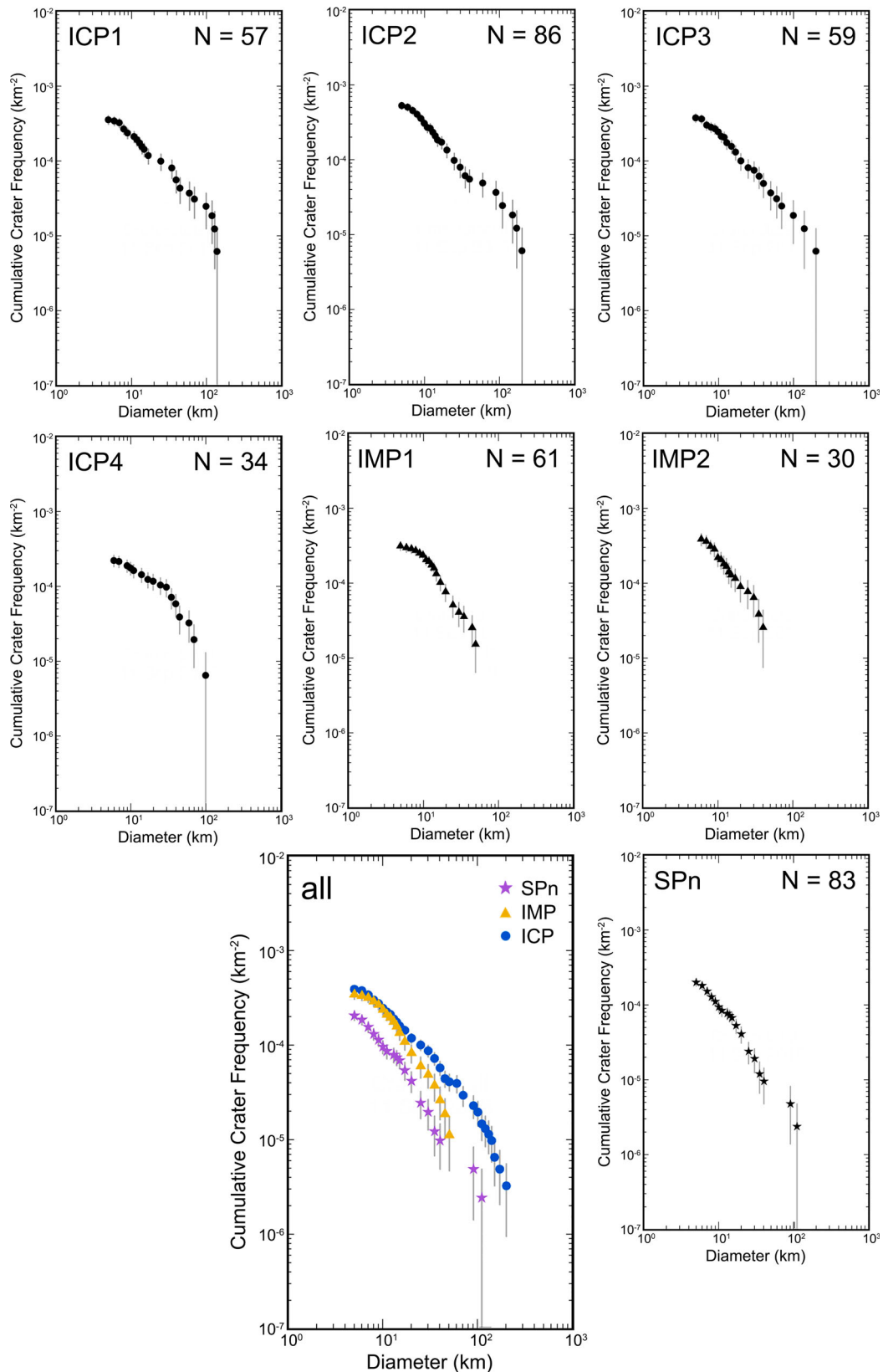
Figure 8. Crater counting results for the seven study areas inside the Victoria quadrangle (i.e. ICP1–ICP4, IMP1, IMP2 and SPn), where N is the number of counted craters. The larger CSFD diagram shows a comparison between the three units (the results from ICP1–4 and IMP1–2 were merged together).

icp, ICP material: rough or gently rolling surfaces, densely cratered and superposed by all three crater classes. These materials encompass distal crater ejecta,

all the older unrecognisable crater materials and subdued secondary clusters and chains. They have a sharp contact with *spn* and a gradational contact with

Table 2. Crater frequencies of the study areas.

Area name	Unit description	A (km^2)	n(5) ± σ	n(10) ± σ	n(20) ± σ	N(5) ± σp	N(10) ± σp	N(20) ± σp
SPn	Northern smooth plains, NE	4.2×10^5	83 ± 9	39 ± 6	17 ± 4	198 ± 22	93 ± 15	40 ± 10
IMP1	Intermediate plains, E	2.0×10^5	61 ± 8	46 ± 7	15 ± 4	308 ± 39	232 ± 34	76 ± 20
IMP2	Intermediate plains, W	7.9×10^5	30 ± 5	17 ± 4	7 ± 3	382 ± 70	216 ± 52	89 ± 34
IMP	Intermediate Plains, all areas	2.8×10^5	91 ± 10	63 ± 8	22 ± 5	329 ± 34	228 ± 29	80 ± 17
ICP1	Intercrater Plains, NW	1.6×10^5	57 ± 8	34 ± 6	16 ± 4	362 ± 48	216 ± 37	102 ± 25
ICP2	Intercrater Plains, central	1.6×10^5	94 ± 10	53 ± 7	24 ± 5	553 ± 60	322 ± 45	142 ± 30
ICP3	Intercrater Plains, E	1.6×10^5	59 ± 8	38 ± 6	16 ± 4	380 ± 49	251 ± 40	103 ± 26
ICP4	Intercrater Plains, SW	1.6×10^5	36 ± 6	27 ± 5	18 ± 4	211 ± 36	167 ± 32	111 ± 26
ICP	Intercrater Plains, all areas	6.3×10^5	246 ± 16	152 ± 12	74 ± 9	375 ± 24	238 ± 19	114 ± 13

Notes: A: actual size of the counting areas in Figure 8. n(D): actual number of craters with diameters ≥D (5, 10 or 20 km) counted within the reference areas in Figure 8. σ: standard error for counted craters, $[N(D)]^{1/2}$ (Crater Analysis Techniques Working Group, 1979). N(D): n(D) normalised to an area of 10^6 km^2, $[n(D)*A]/10^6$. σp: error propagation for the normalised counted craters, $\{[n(D)]^{1/2} \times A\}/10^6$.

imp. Lobate scarps and high-relief ridges are widespread on this unit. *Type-areas:* 318.4°E, 39.6°N; 325.6°E, 63.6°N (Figure 4).

4.4. Relative age estimation

The geologic map of quadrangle H02 provides a database of craters with a diameter size larger than 5 km (Figure 7) up to the largest crater Vyasa (260 km, 275.35°E; 49.20°N). We used this database to estimate the units' ages following the methods described in Crater Analysis Techniques Working Group (1979) and Neukum (1983) to build cumulative size-frequency distribution (CSFD) diagrams of the seven areas shown in Figure 8.

A schematic view of the frequencies of craters with diameter ≥D (i.e. 5, 10 and 20 km) is shown in Table 2, where values are also normalised to an area of 1×10^6 km^2 and presented with their standard error (see Crater Analysis Techniques Working Group, 1979). While SPn values support a clear distinction in age with respect to the other units, ICP and IMP overlap for N(5) and N(10) values. This may be caused both by a bias due to counted secondary craters and by an actual age overlapping between the two units. The IMP unit seems to maintain a distinct intermediate age only for N(20) values. This is apparent also in the plotted crater counting data shown in Figure 8, where IMP craters ≥20 km plot well below ICP confirming a younger age.

4.5. Correlation of main units

Based on the above considerations, we propose the stratigraphic scheme shown in Figure 9 as a summary of the main units mapped in the quadrangle. In this scheme, crater materials are drawn with a breccia-like texture, representing their simple stratigraphic order,
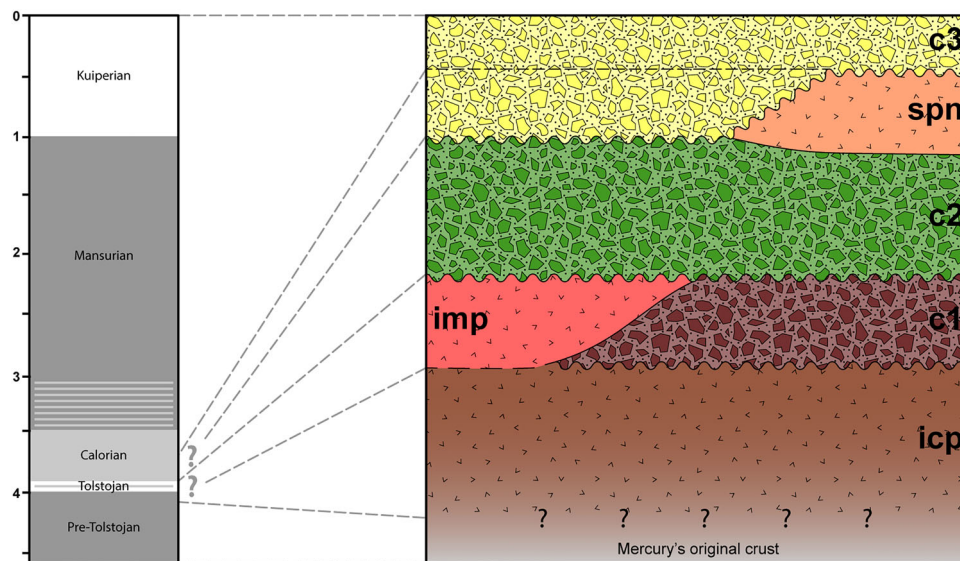

Figure 9. On the right: stratigraphic column showing the correlation of map main units based on observed superposition relationships: undulated contacts represent an erosional relationship; brecciated texture represents generic crater materials pertaining to one of the three crater classes. On the left: time-stratigraphic system for Mercury modified from van Gasselt and Neukum (2011), the dashes inside the solid colours indicate approximate boundaries between periods. The dashed grey lines correlate the map units to the Mercurian periods, based on the estimated ages of SPn, IMP and ICP in literature (Marchi et al., 2013; Neukum, Oberst, Hoffmann, Wagner, & Ivanov, 2001; Ostrach et al., 2015; Whitten et al., 2014) and on the observed relationships. Question marks indicate unclear time relationships between units. A more complete and schematic correlation of all mapped units is shown in the Main Map.

rather than all the possible superposition relationships among continuous crater ejecta found in the quadrangle (e.g. *c3* craters superposing *c1* craters are not represented).

Figure 9 stresses the importance of using the three crater classes as stratigraphic markers to assess the units' relative ages. ICP are confirmed to be the oldest unit, the IMP relative age is constrained by the superposition of crater classes (i.e. only *c2* and *c3*), while the northern SP are confirmed to be the youngest unit sealed on top only by *c1* craters. However, this regional scale stratigraphic scheme may not hold true for the entire planet.

5. Conclusions

We produced the Main Map presented here using MESSENGER data. The average mapping scale of 1:450,000 was chosen to take advantage of the best basemap images available. This represents the first complete geological survey of the Victoria quadrangle and covers the areas left unmapped in the previous M10 map by McGill and King (1983). The results address the importance of further investigating the IMP unit that, at this mapping scale, is morphologically distinguishable from the ICP unit and has a distinct N(20) frequency value (bulk: 80 ± 17) in comparison with the SP unit (40 ± 10) and the ICP unit (bulk: 114 ± 13). This geologic survey will be a support to future local-scale advanced studies, operation simulations and targeting choices for the remote sensing instruments on-board the future ESA-JAXA (European Space Agency, Japan Aerospace eXploration Agency) BepiColombo mission to Mercury.

Software

We used ESRI ArcGIS during map production. Some images were processed using ISIS3 (Integrated Software for Imagers and Spectrometers v3; Eliason, 1997; Gaddis et al., 1997; Torson & Becker, 1997, software developed by the USGS, United States Geological Survey). For crater counting and plotting purposes we used Crater Tools (Kneissl, Van Gasselt, & Neukum, 2011) and Craterstats2 (e.g. see Michael & Neukum, 2010). We also made use of 'Tools for Graphics and Shapes' and 'Polar Plots' by Jenness Enterprises (Jenness, 2011, 2014).

Acknowledgements

Disclosure statement

Funding

ORCiD

V. Galluzzi ⓘ http://orcid.org/0000-0002-3237-3456
G. Di Achille ⓘ http://orcid.org/0000-0002-2151-4057
P. Palumbo ⓘ http://orcid.org/0000-0003-2323-9228

References

Arthur, D. W. G., Agnieray, A. P., Horvath, R. A., Wood, C. A., & Chapman, C. R. (1963). The system of lunar craters, quadrant I. *Communications of the Lunar and Planetary Laboratory*, 2, 71–78, bibcode: 1964CoLPL … 2 … 71A.

Baker, D. M., & Head, J. W. (2013). New morphometric measurements of craters and basins on Mercury and the Moon from MESSENGER and LRO altimetry and image data: An observational framework for evaluating models of peak-ring basin formation. *Planetary and Space Science*, 86, 91–116. doi:10.1016/j.pss.2013.07.003

Becker, K. J., Robinson, M. S., Becker, T. L., Weller, L. A., Turner, S., Nguyen, L., … Solomon, S. C. (2009). Near global mosaic of Mercury. *AGU Fall Meeting Abstracts*, 1, 1189, bibcode: 2009AGUFM.P21A1189B.

Blewett, D. T. (2015). Hollows (Mercury). In H. Hargitai & Á. Kereszturi (Eds.), *Encyclopedia of planetary landforms* (pp. 935–937). New York: Springer. doi:10.1007/978-1-4614-3134-3

Blewett, D. T., Chabot, N. L., Denevi, B. W., Ernst, C. M., Head, J. W., Izenberg, N. R., … Hurwitz, D. M. (2011). Hollows on Mercury: MESSENGER evidence for geologically recent volatile-related activity. *Science*, 333(6051), 1856–1859. doi:10.1126/science.1211681

Byrne, P. K., Klimczak, C., Şengör, A. C., Solomon, S. C., Watters, T. R., & Hauck, S. A. (2014). Mercury's global contraction much greater than earlier estimates. *Nature Geoscience*, 7(4), 301–307. doi:10.1038/ngeo2097

Cintala, M. J., Head, J. W., & Mutch, T. A. (1976). Characteristics of fresh martian craters as a function of diameter: Comparison with the Moon and Mercury. *Geophysical Research Letters*, 3(3), 117–120. doi:10.1029/GL003i003p00117

Crater Analysis Techniques Working Group. (1979). Standard techniques for presentation and analysis of crater size-frequency data. *Icarus*, 37(2), 467–474. doi:10.1016/0019-1035(79)90009-5

Davies, M. E., Dwornik, S. E., Gault, D. E., & Strom, R. G. (1978). *Atlas of Mercury*. NASA Special Publication, 423, bibcode: 1978NASSP.423 … D.

Deetz, C. H., & Adams, O. S. (1945). *Elements of map projection with applications to map and chart construction* (4th ed.). *Special publication* (U.S. Coast and Geodetic Survey),

68 (5th ed.). Washington: US Government Printing Office.

De Hon, R. A., Scott, D. H., & Underwood, J. R., Jr. (1981). *Geologic map of the Kuiper Quadrangle of Mercury*. US Geological Survey, Map I-1233.

Denevi, B. W., Ernst, C. M., Meyer, H. M., Robinson, M. S., Murchie, S. L., Whitten, J. L., … Peplowski, P. N. (2013). The distribution and origin of smooth plains on Mercury. *Journal of Geophysical Research: Planets*, *118* (5), 891–907. doi:10.1002/jgre.20075

Denevi, B. W., Ernst, C. M., Prockter, L. M., Robinson, M. S., Spudis, P. D., Klima, R. L., … Kinczyk, M. J. (2016). *The origin of Mercury's oldest surfaces and the nature of intercrater plains resurfacing*. In Lunar and Planetary Science Conference, 47th, #1624, bibcode: 2016LPI … 47.1624D.

Denevi, B. W., Robinson, M. S., Solomon, S. C., Murchie, S. L., Blewett, D. T., Domingue, D. L., … Chabot, N. L. (2009). The evolution of Mercury's crust: A global perspective from MESSENGER. *Science*, *324*(5927), 467–474. doi:10.1126/science.1172226

Di Achille, G., Popa, C., Massironi, M., Mazzotta Epifani, E., Zusi, M., Cremonese, G., & Palumbo, P. (2012). Mercury's radius change estimates revisited using MESSENGER data. *Icarus*, *221*(1), 456–460. doi:10.1016/j.icarus.2012.07.005

Eliason, E. M. (1997). *Production of digital image models using the ISIS system*. In *Lunar and Planetary Science Conference*, 28th, #1198, bibcode: 1997LPI … 28..331E.

Ernst, C. M., Murchie, S. L., Barnouin, O. S., Robinson, M. S., Denevi, B. W., Blewett, D. T., … Roberts, J. H. (2010). Exposure of spectrally distinct material by impact craters on Mercury: Implications for global stratigraphy. *Icarus*, *209*(1), 210–223. doi:10.1016/j.icarus.2010.05.022

Fassett, C. I., Head, J. W., Blewett, D. T., Chapman, C. R., Dickson, J. L., Murchie, S. L., Watters, T. R. (2009). Caloris impact basin: Exterior geomorphology, stratigraphy, morphometry, radial sculpture, and smooth plains deposits. *Earth and Planetary Science Letters*, *285*(3), 297–308. doi:10.1016/j.epsl.2009.05.022

Frigeri, A., Federico, C., Pauselli, C., & Coradini, A. (2009). *Fostering digital geologic maps: The digital geologic map of Mercury from the USGS atlas of Mercury, geologic series*. In Lunar and Planetary Science Conference, 40th, #2417, bibcode: 2009LPI … 40.2417F.

Gaddis, L., Anderson, J., Becker, K., Becker, T., Cook, D., Edwards, K., … Torson, J. (1997). *An overview of the integrated software for imaging spectrometers (ISIS)*. In Lunar and Planetary Science Conference, 28th, #1226, bibcode: 1997LPI … 28..387G.

van Gasselt, S., & Neukum, G. (2011). Chronology, cratering and stratigraphy. In M. Gargaud, W. M. Irvine, R. Amils, H. J. Cleaves, D. L. Pinti, J. Cernicharo Quintanilla, … M. Viso (Eds.), *Encyclopedia of astrobiology* (pp. 304–313). Berlin/Heidelberg: Springer-Verlag. ISBN: 9783642112713.

Grolier, M. J., & Boyce, J. (1984). *Geologic map of the Borealis region of Mercury*. US Geological Survey, Map I-1660.

Guest, J. E., & Greeley, R. (1983). *Geologic map of the Shakespeare Quadrangle of Mercury*. US Geological Survey, Map I-1408.

Head, J. W., Chapman, C. R., Strom, R. G., Fassett, C. I., Denevi, B. W., Blewett, D. T., … Nittler, L. R. (2011). Flood volcanism in the northern high latitudes of Mercury revealed by MESSENGER. *Science*, *333*(6051), 1853–1856. doi:10.1126/science.1211997

Jenness, J. (2011). *Tools for graphics and shapes: Extension for ArcGIS*. Jenness Enterprises. Retrieved from http://www.jennessent.com/arcgis/shapes_graphics.htm

Jenness, J. (2014). *Polar plots for ArcGIS*. Jenness Enterprises. Retrieved from http://www.jennessent.com/arcgis/polar_plots.htm

Kiefer, W. S., & Murray, B. C. (1987). The formation of Mercury's smooth plains. *Icarus*, *72*(3), 477–491. doi:10.1016/0019-1035(87)90046-7

Kinczyk, M. J., Prockter, L. M., Chapman, C. R., & Susorney, H. C. M. (2016). *A morphological evaluation of crater degradation on Mercury: Revisiting crater classification using MESSENGER data*. In Lunar and Planetary Science Conference, 47th, #1573, bibcode: 2016LPI … 47.1573 K.

King, J. S., & Scott, D. H. (1990). *Geologic map of the Beethoven Quadrangle of Mercury*. US Geological Survey, Map I-2048.

Kneissl, T., Van Gasselt, S., & Neukum, G. (2011). Map-projection-independent crater size-frequency determination in GIS environments – New software tool for ArcGIS. *Planetary and Space Science*, *59*(11), 1243–1254. doi:10.1016/j.pss.2010.03.015

Korteniemi, J., Walsh, L. S., & Hughes, S. S. (2015). Wrinkle ridge. In H. Hargitai & Á. Kereszturi (Eds.), *Encyclopedia of planetary landforms* (pp. 2324–2331). New York: Springer. doi:10.1007/978-1-4614-3134-3

Leake, M. A. (1982). The intercrater plains of Mercury and the Moon: Their nature, origin, and role in terrestrial planet evolution. *Advances in Planetary Geology*, *1*, 3–535. bibcode: 1982apg..book … 3L.

Marchi, S., Chapman, C. R., Fassett, C. I., Head, J. W., Bottke, W. F., & Strom, R. G. (2013). Global resurfacing of Mercury 4.0-4.1 billion years ago by heavy bombardment and volcanism. *Nature*, *499*(7456), 59–61. doi:10.1038/nature12280

Massironi, M., & Byrne, P. K. (2015). High-relief ridge. In H. Hargitai & Á. Kereszturi (Eds.), *Encyclopedia of planetary landforms* (pp. 932–934). New York: Springer. doi:10.1007/978-1-4614-3134-3

Massironi, M., Byrne, P. K., & van der Bogert, C. H. (2015). Lobate scarp. In H. Hargitai & Á. Kereszturi (Eds.), *Encyclopedia of planetary landforms* (pp. 1255–1262). New York: Springer. doi:10.1007/978-1-4614-3134-3

McCauley, J. F., Guest, J. E., Schaber, G. G., Trask, N. J., & Greeley, R. (1981). Stratigraphy of the caloris basin, Mercury. *Icarus*, *47*(2), 184–202. doi:10.1016/0019-1035(81)90166-4

McCauley, J. F., & Wilhelms, D. E. (1971). Geological provinces of the near side of the Moon. *Icarus*, *15*(3), 363–367. doi:10.1016/0019-1035(71)90114-X

McGill, G. E., & King, E. A. (1983). *Geologic map of the Victoria Quadrangle of Mercury*. US Geological Survey, Map I-1409.

Michael, G. G., & Neukum, G. (2010). Planetary surface dating from crater size–frequency distribution measurements: Partial resurfacing events and statistical age uncertainty. *Earth and Planetary Science Letters*, *294*(3), 223–229. doi:10.1016/j.epsl.2009.12.041

Murchie, S., Mick, A., Prockter, L., Rivkin, A., Guinness, E., & Ward, J. (2016). *MDIS CDR/RDR software interface specification*. MESSENGER Online document, v. 1.2.21, Link: http://pdsimage.wr.usgs.gov/data/mess-h-mdis-5-rdr-bdr-v1.0/MSGRMDS_4001/DOCUMENT/MDIS_CDR_RDRSIS.PDF

Murray, B. C., Belton, M. J., Danielson, G. E., Davies, M. E., Gault, D. E., Hapke, B., … Trask, N. (1974). Mercury's surface: Preliminary description and interpretation from Mariner 10 pictures. *Science*, *185*(4146), 169–179. doi:10.1126/science.185.4146.169

Murray, B. C., Strom, R. G., Trask, N. J., & Gault, D. E. (1975). Surface history of Mercury: Implications for terrestrial planets. *Journal of Geophysical Research*, *80*(17), 2508–2514. doi:10.1029/JB080i017p02508

Neukum, G. (1983). *Meteoritenbombardement und Datierung planetarer Oberflächen* (Habilitation thesis for Faculty Membership). Univ. of Munich, 1-186. Translation in: 'Meteorite bombardment and dating of planetary surfaces', NASA TM-77558, 1–158, 1984.

Neukum, G., Oberst, J., Hoffmann, H., Wagner, R., & Ivanov, B. A. (2001). Geologic evolution and cratering history of Mercury. *Planetary and Space Science*, *49*, 1507–1521. doi:10.1016/S0032-0633(01)00089-7

Ostrach, L. R., Robinson, M. S., Denevi, B. W., & Thomas, P. C. (2011). *Effects of incidence angle on crater counting observations*. In Lunar and Planetary Science Conference, 42nd, #1202, bibcode: 2011LPI … 42.1202O.

Ostrach, L. R., Robinson, M. S., Whitten, J. L., Fassett, C. I., Strom, R. G., Head, J. W., & Solomon, S. C. (2015). Extent, age, and resurfacing history of the northern smooth plains on Mercury from MESSENGER observations. *Icarus*, *250*, 602–622. doi:10.1016/j.icarus.2014.11.010

Pohn, H. A., & Offield, T. W. (1970). *Lunar crater morphology and relative-age determination of lunar geologic units – Part 1. Classification*. US Geological Survey Prof. Paper, 153–162.

Preusker, F., Oberst, J., Head, J. W., Watters, T. R., Robinson, M. S., Zuber, M. T., & Solomon, S. C. (2011). Stereo topographic models of Mercury after three MESSENGER flybys. *Planetary and Space Science*, *59*(15), 1910–1917. doi:10.1016/j.pss.2011.07.005

Prockter, L. M., Ernst, C. M., Denevi, B. W., Chapman, C. R., Head, J. W., Fassett, C. I., … Massironi, M. (2010). Evidence for young volcanism on Mercury from the third MESSENGER flyby. *Science*, *329*(5992), 668–671. doi:10.1126/science.1188186

Prockter, L. M., Kinczyk, M. J., Byrne, P. K., Denevi, B. W., Head III, J. W., Fassett, C. I., … the MESSENGER Mapping Group. (2016). *The first global Geological Map of Mercury*. In Lunar and Planetary Science Conference, 47th, #1245, bibcode: 2016LPI … 47.1245P.

Schaber, G. G., & McCauley, J. F. (1980). *Geologic Map of the Tolstoj Quadrangle of Mercury*. US Geological Survey, Map I-1199.

Spudis, P. D., & Guest, J. E. (1988). Stratigraphy and geologic history of Mercury. In F. Vilas, C. R. Chapman, & M. S. Matthews (Eds.), *Mercury* (pp. 118–164). Tucson: University of Arizona Press. ISBN: 0816510857.

Spudis, P. D., & Prosser, J. G. (1984). *Geologic map of the Michelangelo Quadrangle of Mercury*. US Geological Survey, Map I-1659.

Strom, R. G. (1977). Origin and relative age of lunar and mercurian intercrater plains. *Physics of the Earth and Planetary Interiors*, *15*(2), 156–172. doi:10.1016/0031-9201(77)90028-0

Strom, R. G., Banks, M. E., Chapman, C. R., Fassett, C. I., Forde, J. A., Head III, J. W., … Solomon, S. C. (2011). Mercury crater statistics from MESSENGER flybys: Implications for stratigraphy and resurfacing history. *Planetary and Space Science*, *59*(15), 1960–1967. doi:10.1016/j.pss.2011.03.018

Strom, R. G., Chapman, C. R., Merline, W. J., Solomon, S. C., & Head, J. W. (2008). Mercury cratering record viewed from MESSENGER's first flyby. *Science*, *321*(5885), 79–81. doi:10.1126/science.1159317

Strom, R. G., Malin, M. C., & Leake, M. A. (1990). *Geologic map of the Bach Quadrangle of Mercury*. US Geological Survey, Map I-2015.

Strom, R. G., Trask, N. J., & Guest, J. E. (1975). Tectonism and volcanism on Mercury. *Journal of Geophysical Research*, *80*(17), 2478–2507. doi:10.1029/JB080i017p02478

Tanaka, K. L., Skinner Jr., J. A., & Hare, T. M. (2011). *Planetary geologic mappers handbook*. USGS Astrogeology Science Center. Retrieved from http://astrogeology.usgs.gov/search/details/Docs/Mappers/PGM_Handbook_2011/pdf

Thomas, R. J., Rothery, D. A., Conway, S. J., & Anand, M. (2014a). Hollows on Mercury: Materials and mechanisms involved in their formation. *Icarus*, *229*, 221–235. doi:10.1016/j.icarus.2013.11.018

Tobler, W. (1987). *Measuring spatial resolution*. In Proceedings of the Land Resources Information Systems Conference, Beijing, 12–16.

Torson, J. M., & Becker, K. J. (1997). *ISIS – A software architecture for processing planetary images*. In Lunar and Planetary Science Conference, 28th, #1219, bibcode: 1997LPI … 28.1443T.

Trask, N. J., & Dzurisin, D. (1984). *Geologic map of the Discovery Quadrangle of Mercury*. US Geological Survey, Map I-1658.

Trask, N. J., & Guest, J. E. (1975). Preliminary geologic terrain map of Mercury. *Journal of Geophysical Research*, *80*(17), 2461–2477. doi:10.1029/JB080i017p02461

Weider, S. Z., Nittler, L. R., Starr, R. D., Crapster-Pregont, E. J., Peplowski, P. N., Denevi, B. W., … Solomon, S. C. (2015). Evidence for geochemical terranes on Mercury: Global mapping of major elements with MESSENGER's X-Ray spectrometer. *Earth and Planetary Science Letters*, *416*, 109–120. doi:10.1016/j.epsl.2015.01.023

Whitten, J. L., Head, J. W., Denevi, B. W., & Solomon, S. C. (2014). Intercrater plains on Mercury: Insights into unit definition, characterization, and origin from MESSENGER datasets. *Icarus*, *241*, 97–113. doi:10.1016/j.icarus.2014.06.013

Wood, C. A. (1979). *Crater degradation through lunar history*. In *Lunar and Planetary Science Conference*, 10, 1373–1375, bibcode: 1979LPI … 10.1373W.

Wood, C. A., & Anderson, L. (1978). *New morphometric data for fresh lunar craters*. In Lunar and Planetary Science Conference, 9th, 3669–3689, bibcode: 1978LPSC .9.3669W.

Wood, C. A., Head, J. W., & Cintala, M. J. (1977). *Crater degradation on Mercury and the Moon-Clues to surface evolution*. In *Lunar and Planetary Science Conference*, 8th, 3503–3520, bibcode: 1977LPSC … 8.3503W.

Zuber, M. T., Smith, D. E., Phillips, R. J., Solomon, S. C., Neumann, G. A., Hauck II, S. A., … Yang, D. (2012). Topography of the northern hemisphere of Mercury from MESSENGER laser altimetry. *Science*, *336*(6078), 217–220. doi:10.1126/science.1218805